Particle-in-cell simulation for parametric decays of a circularly polarized Alfvén wave in relativistic thermal electron-positron plasma

Rodrigo A. López, Víctor Muñoz, Adolfo F. Viñas, and J. Alejandro Valdivia

Citation: Physics of Plasmas (1994-present) **21**, 032102 (2014); doi: 10.1063/1.4867255
View online: http://dx.doi.org/10.1063/1.4867255
View Table of Contents: http://scitation.aip.org/content/aip/journal/pop/21/3?ver=pdfcov
Published by the AIP Publishing

Particle-in-cell simulation for parametric decays of a circularly polarized Alfvén wave in relativistic thermal electron-positron plasma

Rodrigo A. López,[1,a)] Víctor Muñoz,[1] Adolfo F. Viñas,[2] and J. Alejandro Valdivia[1,3]
[1]*Departamento de Física, Facultad de Ciencias, Universidad de Chile, Casilla 653, Santiago, Chile*
[2]*NASA Goddard Space Flight Center, Heliophysics Science Division, Geospace Physics Laboratory, Mail Code 673, Greenbelt, Maryland 20771, USA*
[3]*Centro para el Desarrollo de la Nanociencia y la Nanotecnología, CEDENNA, Santiago, Chile*

(Received 25 October 2013; accepted 19 February 2014; published online 4 March 2014)

Parametric decays of a left-handed circularly polarized Alfvén wave propagating along a constant background magnetic field in a relativistic thermal electron-positron plasma are studied by means of a one dimensional relativistic particle-in-cell simulation. Relativistic effects are included in the Lorentz equation for the momentum of the particles and in their thermal motion, by considering a Maxwell-Jüttner velocity distribution function for the initial condition. In the linear stage of the simulation, we find many instabilities that match the predictions of relativistic fluid theory. In general, the growth rates of the instabilities increase as the pump wave amplitude is increased, and decrease with a raise in the plasma temperatures. We have confirmed that for very high temperatures the Alfvén branch is suppressed, consistent with analytical calculations. © *2014 AIP Publishing LLC*.
[http://dx.doi.org/10.1063/1.4867255]

I. INTRODUCTION

There are several environments in which relativistic electron-positron plasmas are relevant. Examples of these environments are high-energy astrophysical plasmas such as pulsar magnetospheres,[1,2] active galactic nuclei,[3,4] gamma-ray bursts,[5,6] and models of early universe.[7,8] Recently, electron-positron plasmas have become relevant in laboratory plasmas by means of ultra-intense lasers[9] and tokamaks.[10,11]

Several effects in these plasmas are related to wave propagation, such as the proposed pulsar radio emission processes,[12] bulk acceleration of relativistic jets,[13] and quasar relativistic jets,[14] among others. When these plasmas have strong magnetic fields, Alfvén waves should play a fundamental role, e.g., they are the ubiquitous byproduct of magnetic reconnection in space, astrophysical and laboratory plasmas as evidenced by *in situ* spacecraft observations in the solar wind.[15–17] Recently, there is a growing interest in the study of these Alfvén waves in relativistic electron-positron plasmas, not only related to magnetic reconnection[18–22] but also their nonlinear evolution as a general scientific problem, motivated by potential applications in astrophysics and laboratory environments.[14,23–26]

For example, in the magnetosphere of pulsars, particularly in millisecond pulsars, there must be large electric fields that can accelerate charged particles along the magnetic field. In these environments, the particle number density is expected to be of order $10^{17}\,\mathrm{cm}^{-3}$, with magnetic fields of order $B \sim 10^{12}\,\mathrm{G}$,[27] values which can increase by an order of magnitude under dynamical situations.[28] In magnetars, where $B > 4 \times 10^{13}\,\mathrm{G}$, number density can be even larger, due to other important effects in the production of electron-positron pairs, such as photon splitting in a strong magnetic field[2] or electron-positron pair annihilation into a photon in the presence of a strong magnetic field.[29] For instance, Da Costa *et al.*[30] used a value of $n_e = 10^{17}\,\mathrm{cm}^{-3}$, while Matsukiyo and Hada[31] used $\Omega^2/\omega_{pe}^2 = 0.1$ with $\Omega = eB/mc$ and $\omega_{pe} = \sqrt{4\pi n_e e^2/m}$.

Given the extreme conditions of these environments, it becomes important to study the nonlinear evolution of these Alfvén waves. In electron-positron plasmas, the parametric decays of a circularly polarized Alfvén waves have been studied in the weakly relativistic limit by means of two fluid theory[32] and particle-in-cell (PIC) simulations.[33] It has been found that the successive parametric instabilities result in turbulent wave forms. Using particle-in-cell simulations, the long time evolution of parametric instabilities of large amplitude Alfvén waves has been studied for an electron-positron plasma,[31] where the successive parametric instabilities develop in an efficient particle acceleration process. In these papers, the authors consider a nonrelativistic temperature regime. However, in the astrophysical and laboratory environments mentioned above, the effects of relativistic temperatures may play a very important role,[34] as suggested by the analytical results of a relativistic two fluid thermal electron-positron plasma.[35] Hence, in the present paper we study the parametric instabilities of a circularly polarized Alfvén wave in a fully relativistic thermal electron-positron plasma by means of a one dimensional particle-in-cell simulation. The results are compared with the analytical solutions obtained in Ref. 35 for a two fluid thermal electron-positron plasma. Here, the relativistic temperature effects are included by means of a Maxwell-Jüttner velocity distribution for the initial condition.

The paper is organized as follows. In Sec. II, a review of the parametric decays of a left-handed circularly polarized Alfvén wave in a relativistic electron-positron plasma is briefly presented. This review is based on the results of Ref. 35. In Sec. III, the numerical particle-in-cell simulation used is described. Then, in Sec. IV, the results of the

a)rlopez186@gmail.com

simulation are presented and compared with the fluid model predictions. Finally, in Sec. VI, results are summarized and conclusions are outlined.

II. PARAMETRIC DECAYS

In Ref. 35, the authors studied the parametric decays of a left-handed circularly polarized Alfvén wave in a relativistic thermal electron-positron plasma, propagating along a constant background magnetic field. The exact dispersion relation for the pump wave was calculated within the context of a relativistic fluid theory.[36] Since the pump wave has left-handed polarization, the electromagnetic fields can be written as

$$\vec{E}_0(X,t) = E[\sin(k_0X - \omega_0 t)\hat{y} - \cos(k_0X - \omega_0 t)\hat{z}], \quad (1)$$

$$\vec{B}_0(X,t) = B[\cos(k_0X - \omega_0 t)\hat{y} + \sin(k_0X - \omega_0 t)\hat{z}] + B_{0X}\hat{X}, \quad (2)$$

where E and B are the amplitude of the monochromatic electromagnetic wave, ω_0 and k_0 are its frequency and wave number, respectively, and B_{0X} is the constant background magnetic field. This circularly polarized electromagnetic wave is an exact nonlinear solution of the fluid equations, with the corresponding purely transverse quiver velocities given by

$$v_{\perp 0j} = v_{y0j} + iv_{z0j} = -\eta_j\left(\frac{\omega_0\,\alpha}{f_{0j}\gamma_{0j}\omega_0 - \Omega_{cj}}\right)e^{i(k_0X-\omega_0 t)}, \quad (3)$$

where j is the species index ($j=e$ for electrons and $j=p$ for positrons), $\eta_e = -1$, $\eta_p = 1$, $\gamma_{0j} = (1 - |v_{\perp 0j}|^2/c^2)^{-1/2}$ is the relativistic factor, and $\Omega_c \equiv \Omega_{cp} = -\Omega_{ce}$ is the positron gyrofrequency. The normalized pump wave amplitude is $\alpha = eA/(mc^2)$, where A is the amplitude of the vector potential of the wave. We can write α in terms of E or B, using Eqs. (1), (2), and Maxwell's equations. Finally, f_j is a relativistic thermal factor which is related to the temperature by $f_j = K_3(\mu_j)/K_2(\mu_j)$ (for a Maxwell-Jüttner relativistic distribution), where $\mu_j = mc^2/(k_B T_j)$, and K_2 and K_3 are the modified Bessel functions of order 2 and 3, respectively.

The exact dispersion relation for the pump wave is given by

$$\omega_0^2 - c^2k_0^2 = \omega_{pe}^2\left(\frac{\omega_0}{f_{0}\gamma_{0e}\omega_0 + \Omega_c} + \frac{\omega_0}{f_{0}\gamma_{0p}\omega_0 - \Omega_c}\right), \quad (4)$$

where $\omega_{pe}^2 = 4\pi ne^2/m$ is the electron plasma frequency, with $n_{0e} = n_{0p} = n$ as the electron/positron density in the lab frame. We have assumed thermal equilibrium, so that $T_{0e} = T_{0p} = T_0$ is constant, hence $\mu_{0e} = \mu_{0p} = \mu_0$ is also constant, and also $f_{0e} = f_{0p} = f_0$. In Fig. 1, we show the dispersion relation for the pump wave equation (4) for various values of α. There are four branches: two electromagnetic branches, with a lower cutoff at the effective plasma frequency; and two Alfvén branches, which have an upper cutoff in frequency, and for $\alpha \neq 0$, an upper cutoff in wave number.

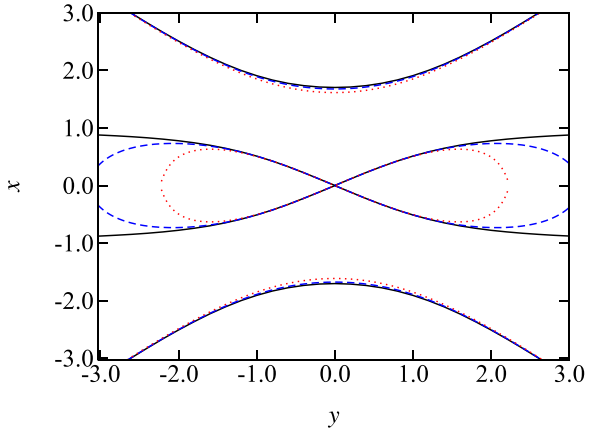

FIG. 1. Dispersion relation for the pump wave equation (4). Normalized wave number $y = ck/\Omega_c$ vs. normalized frequency $x = \omega/\Omega_c$ for $\omega_{pe}/\Omega_c = 1$ and $1/\mu = 0.01$. Solid black line: $\alpha = 0$; dashed blue line: $\alpha = 0.1$; dotted red line: $\alpha = 0.2$.

Now we introduce small longitudinal perturbations of the form $\exp(ikX - i\omega t)$ on the zeroth order solution given by the pump wave described above. The perturbations are for the fields, densities, velocities, and temperatures of each species. After some calculation, we get the nonlinear dispersion relation for the longitudinal perturbations [Eq. (36) in Ref. 35]. When there is no pump wave, $\alpha = 0$, the dispersion relation for the longitudinal perturbations yields the normal linear modes that propagate in the plasma. In this limit, it is not difficult to show that the dispersion relation becomes

$$F_{SD}(k,\omega) = D_+D_-SL = 0, \quad (5)$$

where

$$S = -\omega^2 + v_s^2k^2, \quad (6)$$

$$L = \frac{2\omega_{pe}^2}{f_0} - \omega^2 + v_s^2k^2, \quad (7)$$

$$D_+ = \omega_+^2 - c^2k_+^2 - \omega_{pe}^2\left(\frac{\omega_+}{f_0\omega_+ - \Omega_c} + \frac{\omega_+}{f_0\omega_+ + \Omega_c}\right), \quad (8)$$

$$D_- = \omega_-^{*2} - c^2k_-^{*2} - \omega_{pe}^2\left(\frac{\omega_-^*}{f_0\omega_-^* - \Omega_c} + \frac{\omega_-^*}{f_0\omega_-^* + \Omega_c}\right). \quad (9)$$

Here, $\omega_+ = \omega_0 + \omega, \omega_- = \omega_0 - \omega^*, k_+ = k_0 + k, k_- = k_0 - k^*$, and

$$v_s^2 = \frac{1}{f_0\mu_0}\left(\frac{f_j'(\mu_0)\mu_0^2}{1 + f_j'(\mu_0)\mu_0^2}\right),$$

where $f' = df/d\mu$. This is the effective sound velocity for the relativistic case. Equation (5) shows that the normal modes correspond to an electroacoustic wave (given by $S=0$), Langmuir waves ($L=0$), and sideband electromagnetic waves ($D_\pm = 0$). In the presence of the pump wave ($\alpha \neq 0$), these normal modes couple and give rise to the parametric decays.

The dispersion relation, Eq. (36) in Ref. 35, is solved numerically for the parametric decays. For a given value of α and μ, we choose a value of the normalized wave number of the pump wave, $y_0 = ck_0/\Omega_c$, and we solve the dispersion relation of the pump wave, Eq. (4), to get the normalized pump wave frequency, $x_0 = \omega_0/\Omega_c$.

In Fig. 2, we show the solutions for the dispersion relation for a pump wave in the Alfvén branch. We choose $y_0 = 0.49$, $\omega_{pe}/\Omega_c = 1$, and $\mu = 100$. We solve the dispersion relation for $\alpha = 0$, which is equivalent to solve Eq. (5). There are 12 lines, two of which correspond to the electroacoustic modes that are real solutions of $S = 0$. They are labeled as S_+ and S_-, corresponding to the forward and backward propagating modes, respectively. Two other lines correspond to the Langmuir modes given by $L = 0$, and labeled as L_+ (forward) and L_- (backward). The other eight lines correspond to the eight real solutions of $D_\pm$. Four of these lines are parabolic and correspond to the usual electromagnetic branches in a relativistic plasma.[36] They are labeled as $D_\pm$ in Fig. 2. The two lines $p_\pm$ also correspond to solutions of $D_\pm$, but they resonate at the sideband frequency $\omega_\pm = \Omega_c/f_0$, which in the cold case is the positron gyrofrequency [see Eqs. (8) and (9)]. In terms of the normalized longitudinal frequency $x = \omega/\Omega_c$, the resonance occurs at $x = \pm(-x_0 + 1/f_0)$, as shown in Fig. 2. Similarly, $e_\pm$ are the two solutions which resonate at the sideband frequency $\omega_\pm = -\Omega_c/f_0$ (which in the cold limit, is the electron gyrofrequency), that is, at $x = \pm(-x_0 - 1/f_0)$.

III. SIMULATION SETUP

We have performed a fully relativistic one dimensional PIC simulation, in which we solve the momentum equations of both electrons and positrons in the self-consistent electric and magnetic fields obtained from a solution of Maxwell's equations. Relativistic effects have been included in the Lorentz equation for the particles momentum and in their thermal motions, by considering a Maxwell-Jüttner velocity distribution function[37] for the initial condition, namely,

$$f(u) = \frac{\mu}{c^3 K_2(\mu)} \exp\left[-\mu\left(1 + \frac{u^2}{c^2}\right)^{\frac{1}{2}}\right], \qquad (10)$$

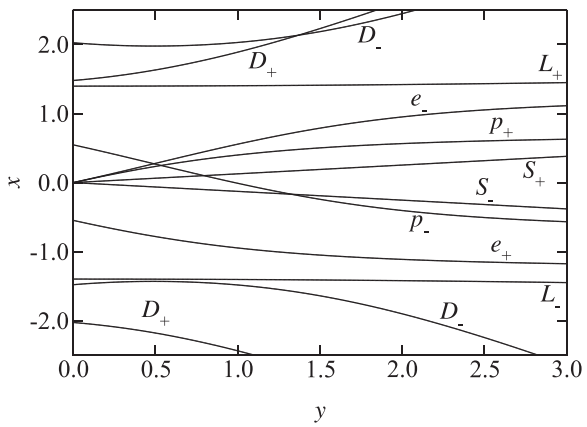

FIG. 2. Solution of the dispersion relation equation (36) in Ref. 35. Normalized wave number $y = ck/\Omega_c$ vs. normalized frequency $x = \omega/\Omega_c$ for $y_0 = 0.49$, $\omega_{pe}/\Omega_c = 1$, $1/\mu = 0.01$, and $\alpha = 0$.

where $u = \gamma v$ is the relativistic momentum per unit mass.

The simulation has only one spatial dimension x and three velocity dimensions are retained. We set the magnetic field in the X direction, so that we study the parallel wave propagation. The spatial boundary conditions for the system are periodic. The details of the simulation are described in Refs. 38–40.

To study the parametric decays of the left-handed circularly polarized Alfvén wave, we choose a pump wave with a normalized wave number $y_0 = 0.49$, and solve the pump wave dispersion relation Eq. (4) to get the normalized frequency $x_0 = 0.27$ for the pump wave at the Alfvén branch.[36] We set the initial electromagnetic fields according to Eqs. (1) and (2), and the initial fluid velocity given by Eq. (3). The initial temperature of the system is set assuming Eq. (10). The system size is $L = 512\, c/\omega_{pe}$, the number of grid points is $n_g = 2048$, and the time step $\omega_{pe}\Delta t = 0.01$. We have used the same number of electron and positrons, with $n_e = n_p = 1000$, initially in each grid. The current J and the charge density ρ at a given position and time are computed using the particle-in-cell method[39,40] with a second order interpolation function.

IV. SIMULATION RESULTS

With the setup described in Sec. III, we run the simulation with an initial pump wave of amplitude $\alpha = 0.2$ and $y_0 = 0.49$, until $\omega_{pe}t = 1310.72$, which allows us to have a power of two for the number of iterations. In Fig. 3, we show the spatiotemporal evolution of the B_y component of the magnetic field. In the early stage of the simulation, $\omega_{pe}t \approx 400$, we only see the presence of the pump wave with a propagation speed that is consistent with the dispersion relation equation (4). At around $\omega_{pe}t \approx 400$, the instabilities start to grow as we observe excited waves that begin to propagate in the opposite direction to the original pump wave. At the end of the simulation, these excited waves become propagating localized structures.

Figure 4(a) shows the power spectrum for the transverse magnetic field fluctuations, for the period $0 \le \omega_{pe}t \le 1310.72$. In this figure, it can be seen the typical dispersion relation for this relativistic plasma with Alfvén and electromagnetic branches (growing from the thermal noise), plus some regions

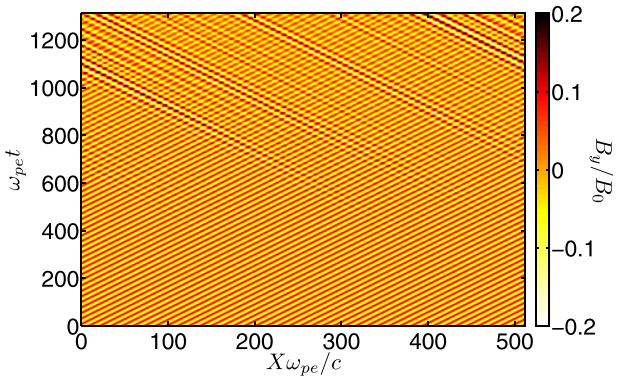

FIG. 3. Spatiotemporal evolution of the y component of the normalized magnetic field. Normalized time $\omega_{pe}t$ vs. normalized space $X\omega_{pe}/c$, for $\mu = 100$, $\alpha = 0.2$, $\omega_{pe}/\Omega_c = 1$, $y_0 = 0.49$.

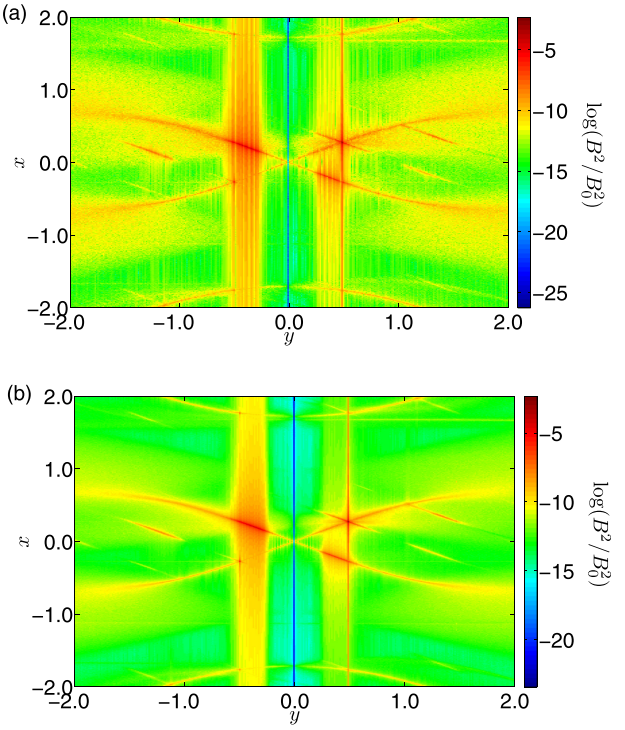

FIG. 4. (a) Power spectrum for the transverse magnetic field fluctuations. Normalized frequency $x = \omega/\Omega_c$ vs. normalized wave number $y = ck/\Omega_c$, for $\mu = 100$, $\alpha = 0.2$, $\omega_{pe}/\Omega_c = 1$, $y_0 = 0.49$. (b) Same plot as before, but taking average over 16 simulations.

where the power is concentrated as we now describe in detail. We note that we can eliminate a lot of the numerical noise in this figure by running several simulations with the same parameters, but with different seeds for the initial velocity distribution, and taking average over the results of the simulations. In Fig. 4(b), we plot the average over 16 simulations for the power spectrum of the transverse magnetic field fluctuations. The main behavior shown in Fig. 4(a) is retained in this figure, which means that it is a robust behavior in the simulation. The numerical noise has been reduced considerably, giving rise to a much smoother figure. From now on, we will use the average quantities for the analysis.

Since the pump wave is a left-handed circularly polarized Alfvén wave, the first quadrant of the dispersion relation in Fig. 4 shows the left-handed forward propagating waves ($\mathcal{L}_f$), while the second quadrant shows the left-handed backward propagating waves ($\mathcal{L}_b$). The third and fourth quadrants show the right-handed forward and backward propagating waves, respectively ($\mathcal{R}_f$, $\mathcal{R}_b$). According to Fig. 4, most of the power resides at the Alfvén branch in the first quadrant $(y, x) \approx (0.49, 0.27)$, which corresponds to the pump wave $\mathcal{L}_f$. We also observe $\mathcal{L}_b$ around $(y, x) \approx (-0.49, 0.27)$ and $\mathcal{R}_b$ $(y, x) \approx (0.49, -0.27)$ Alfvén waves in second and fourth quadrants, respectively, but the $\mathcal{R}_f$ (third quadrant) is not excited.

We decompose the wave data obtained in Fig. 3, into two spiral modes with positive and negative helicity (corresponding to positive and negative wave numbers, respectively) as done in Ref. 41. Therefore, the spiral mode B_y^r with positive helicity ($k > 0$) consists of $\mathcal{L}_f$ and $\mathcal{R}_b$ waves propagating forward and backward, respectively. On the other hand, the spiral mode B_y^l with negative helicity ($k < 0$) consists of $\mathcal{R}_f$ and $\mathcal{L}_b$ waves. In Fig. 5, we show the decomposition of B_y into the two spiral modes. Figure 5(a) shows B_y^r, where we can clearly see the presence of the pump wave, which is a $\mathcal{L}_f$ wave with $y_0 = 0.49$ (i.e., 40 modes in the box with length $L = 512\, c/\omega_{pe}$). Less clear is the presence of the $\mathcal{R}_b$ wave, as we saw in the fourth quadrant of Fig. 4. Figure 5(b) shows B_y^l. Here, we note the presence of the $\mathcal{L}_b$ wave as expected, while the $\mathcal{R}_f$ wave is very weak (as we saw in the third quadrant of Fig. 4). Note that at the beginning of the simulation there is no wave present in Fig. 5(b) since the system is started with a pump wave $\mathcal{L}_f$.

In order to compare the simulation results with the analytical ones, obtained using a relativistic fluid model in Ref. 35, we plot in Fig. 6(a) the dispersion relation of the parametric decays in the fluid model, for $\alpha = 0.2$. We can see from Fig. 2 ($\alpha = 0$) that there are several possible crossings between solutions of the dispersion relation. At these crossings, complex solutions can appear when $\alpha \neq 0$. The presence of complex solutions with positive imaginary frequency implies the presence of unstable waves, corresponding to the parametric decays of the pump wave. The real part of the complex solution with positive imaginary frequency has been plotted as a dotted (red) line in Fig. 6(a). We observe, from the analytical solution, that only three crossings have developed instabilities. The first crossing is a modulational instability[42] close to the origin between (p_+, e_-) [see Fig. 2]. The second crossing is between (S_+, p_-) and corresponds to an ordinary decay instability, in which the pump wave

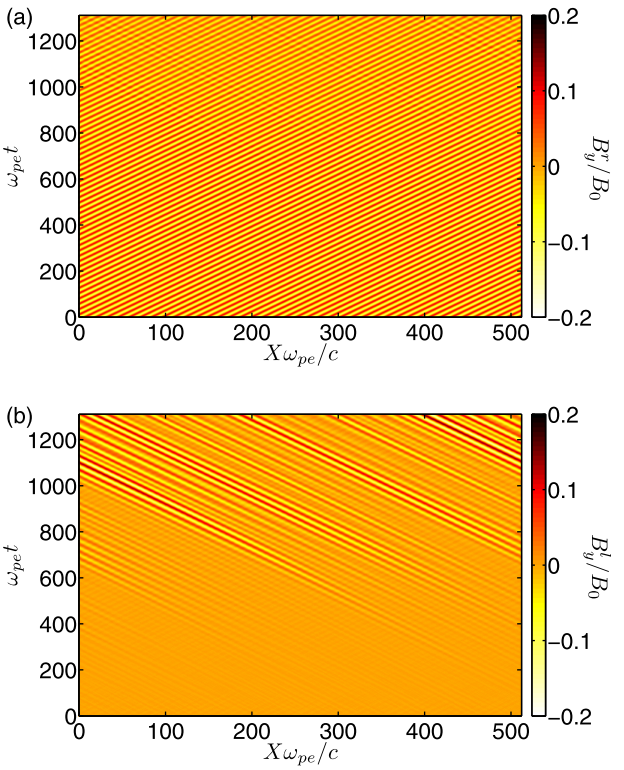

FIG. 5. Spatiotemporal evolution of the y component of the normalized magnetic field. Normalized time $\omega_{pe}t$ vs. normalized space $X\omega_{pe}/c$, for $\mu = 100$, $\alpha = 0.2$, $\omega_{pe}/\Omega_c = 1$, $y_0 = 0.49$. (a) Positive helicity B_y^r, showing $\mathcal{L}_f$ and $\mathcal{R}_b$ waves. (b) Negative helicity B_y^l, showing $\mathcal{L}_b$ and $\mathcal{R}_f$ waves.

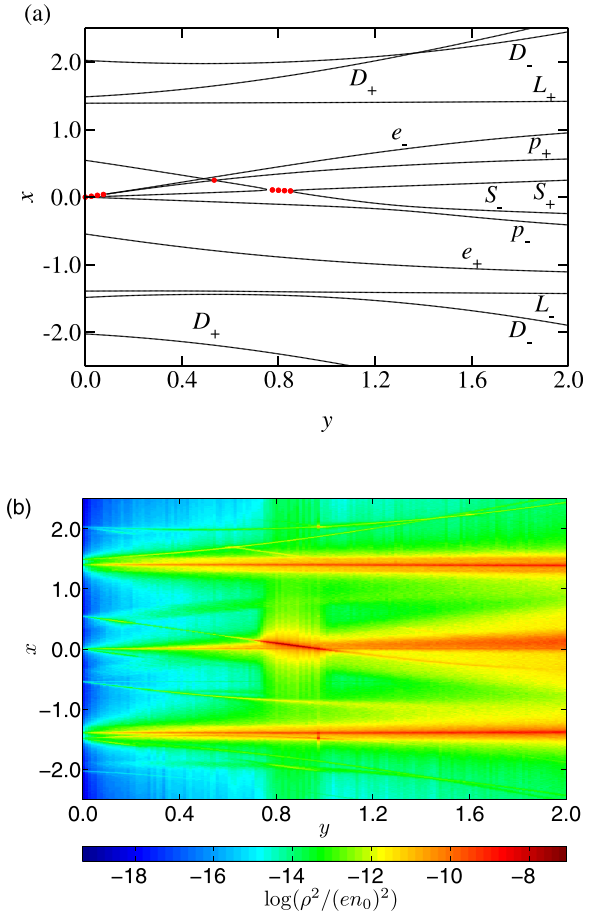

FIG. 6. Dispersion relation x vs. y, for $\mu = 100$, $\alpha = 0.2$, $\omega_{pe}/\Omega_c = 1$, $y_0 = 0.49$. (a) Fluid theory, Eq. (32) in Ref. 35. Dotted lines represent the real part of the solution when it is complex. (b) Power spectrum for the normalized density fluctuations, taking average over 16 simulations.

decays into a forward propagating electroacoustic mode of frequency and wave number (ω, k) and a sideband wave with $(\omega_-^*, k_-^*) = (\omega_0 - \omega, k_0 - k)$. Finally, the third crossing is between (p_+, p_-), in which the pump wave decays into sideband waves p_+ with $(\omega, k) = (\omega_0 + \omega, k_0 + k)$ and p_-. In Fig. 6(a), we see that the instabilities occur at $(x, y) \approx (0, 0.1)$, $(x, y) \approx (0.1, 0.8)$, and $(x, y) \approx (0.25, 0.53)$, respectively.

In Fig. 6(b), we have plotted the power spectrum for the normalized density fluctuations $\rho^2/(en_0)^2$ (taking average over 16 simulations). Comparing this figure with Fig. 6(a), we can identify many of the modes predicted by the fluid model; some of them are more damped than others. There is a clear peak in the power spectrum in the region $0.8 < y < 1$, for $x \sim 0.1$, which is consistent with the prediction of the fluid model for the ordinary decay instability of (S_+, p_-). As we said before, the electromagnetic sideband wave p_- has normalized frequency and wave number $(x_0 - x, y_0 - y)$. Remembering that the pump wave is $(x_0, y_0) = (0.27, 0.49)$ and that the instability occurs at $(x, y) \approx (0 \sim 0.1, 0.8 \sim 1)$, then in the electromagnetic power spectrum there should be a peak in the range $(0 \sim 0.17, -0.31 \sim -0.51)$, which is consistent with Fig. 4. Therefore, the sideband wave p_- is the left-handed backward propagating wave $(\mathcal{L}_b)$ shown in Fig. 5(b). The electroacoustic mode S_+ has frequency and wave number $(x, y) \approx (0 \sim 0.1, 0.8 \sim 1)$.

The modulational instability (p_+, e_-) predicted in Fig. 6(a) has a lower growth rate compared with the instability at (S_+, p_-) [see Ref. 35 or Fig. 9(a) below], hence its effect is not relevant in Fig. 6. The same occurs for the instability at (p_+, p_-). Notice that a strong signal at $(x, y) = (-1.5, 1)$ is also observed in Fig. 6(b), a feature which is not present in the fluid model and which may be due to kinetic effects or nonlinear couplings not considered in our model (notice that our initial condition for the simulation is exact for the fluid theory, but not for the kinetic one).

The temporal evolution of the wave number modes can be seen in Fig. 7. We can observe that for the transverse magnetic fluctuations, Fig. 7(a), the pump wave at $y = 0.49$ is the strongest mode. In the linear stage of the simulation, up to $\omega_{pe}t \approx 300$, the modes at $y \approx -0.3 \sim -0.5$ start to grow, which correspond to the mode p_-, as we saw before. At about the same time, the evolution of the density fluctuation modes, Fig. 7(b), shows growing modes at $y \approx 0.8 \sim 1$, corresponding to the S_+ mode. Modes close to $y \approx 0.49$ in Fig. 7(a) may correspond to the modulational instability (p_+, e_-) at $(x, y) \approx (0, 0.1)$ in Fig. 6(a), because p_+ and p_- satisfy the matching condition at $y_0 + y \approx 0.5$ and $y_0 - y \approx 0.48$, respectively. At the end of the simulation, $\omega_{pe}t \approx 900$ the mode at $y \approx 1$ is slightly excited in Fig. 7(a); this may correspond to the mode p_+ of the decay (p_+, p_-) at $(x, y) \approx (0.25, 0.53)$ in Fig. 6, with wave number $y_0 + y \approx 1.02$. We observe in Fig. 7(a) that at this time there are other active modes in the simulation, which are not expected according to the fluid model. In fact, also in Fig. 6(b), which shows the dispersion relation for the

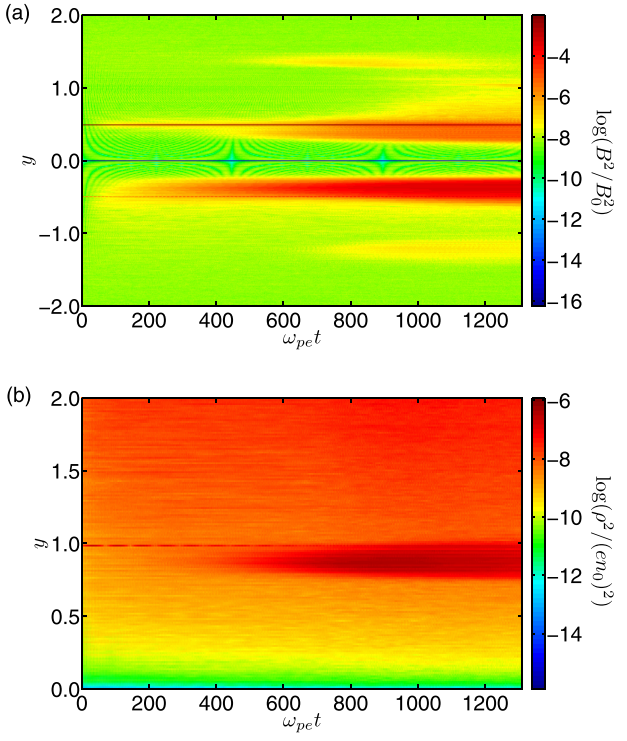

FIG. 7. Temporal evolution of the wave number modes, y vs. $\omega_{pe}t$, for $\mu = 100$, $\alpha = 0.2$, $\omega_{pe}/\Omega_c = 1$, $y_0 = 0.49$. Graphs are obtained by taking an average over 16 simulations. (a) Modes for the transverse magnetic fluctuations. (b) Modes for the density fluctuations.

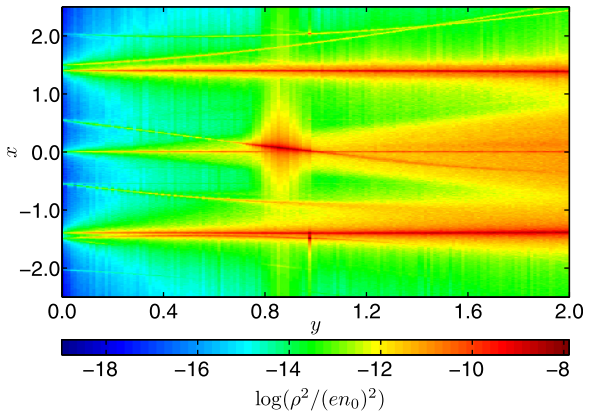

FIG. 8. Power spectrum for the normalized density fluctuations, for $\mu = 100$, $\alpha = 0.2$, $\omega_{pe}/\Omega_c = 1$, $y_0 = 0.49$, $0 \leq \omega_{pe}t \leq 655.36$, taking average over 16 simulations.

parametric decays in the simulation, there are modes which are not described by the fluid model. This may obey to successive decay processes,[33] or to other nonlinear interactions that are becoming apparent in Fig. 5. To illustrate this, in Fig. 8, we plot the power spectrum for the normalized density fluctuation for the same set of parameters as in Fig. 6(b), but considering only half of the simulation time, $0 \leq \omega_{pe}t \leq 655.36$. The modes observed in Fig. 8 are exactly the predicted modes in Fig. 6(a), suggesting that the extra modes in Fig. 6(b) develop at a later stage during the simulation.

In Fig. 7(a), we can also identify a weak mode at $y = -0.49$, growing at the beginning of the simulation. The appearance of this mode is not predicted by the fluid model, and it may be due to the fact that the initial condition is a normal mode for the fluid model, but not necessarily for a kinetic model. However, its amplitude is very weak in comparison with the pump wave, and its presence does not affect the analysis of the parametric decays of the pump wave.

In Fig. 9, we plot the growth rates for the instabilities in this system. Figure 9(a) shows the growth rate for the fluid model, where $\Gamma = \mathrm{Im}(x)$ has a maximum value at $y \approx 0.8$. The instabilities at the origin $y \approx 0.1$, and at $y \approx 0.5$, are very weak. We observe that as we increase the pump wave amplitude, α, the growth rates of the instabilities increase. Fig. 9(b) shows the growth rates calculated in the simulation from the density fluctuation modes in Fig. 7(b), which are calculated by seeking the time period in which the modes

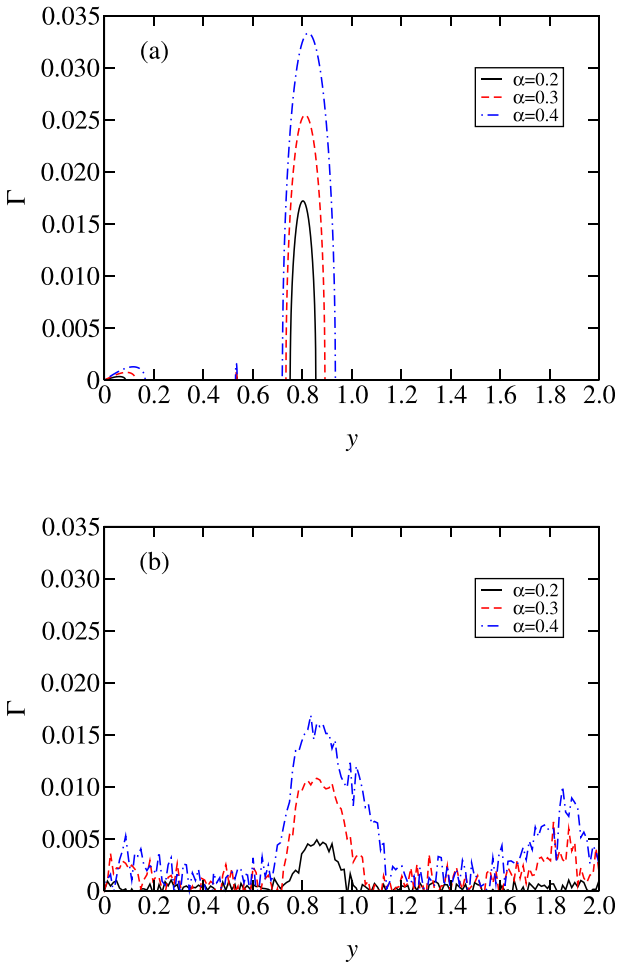

FIG. 9. Growth rates for decays, $\Gamma = \mathrm{Im}(x)$ vs. y, for $\mu = 100$, $\omega_{pe}/\Omega_c = 1$, $y_0 = 0.49$ and x_0 lying in the Alfvén branch. Solid line: $\alpha = 0.2$; dashed line: $\alpha = 0.3$; dotted dashed line: $\alpha = 0.4$. (a) Fluid theory in Ref. 35. (b) Growth rates of the density fluctuation modes in the simulation, taking average over 16 simulations.

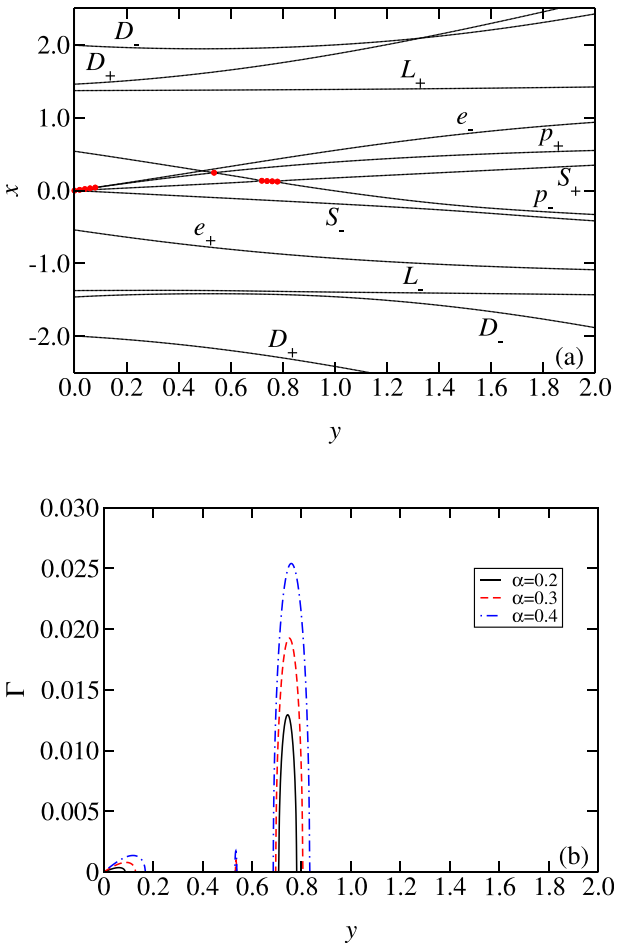

FIG. 10. (a) Dispersion relation x vs. y for the fluid theory, Eq. (32) in Ref. 35, for $\alpha = 0.2$, $\mu = 50$, $\omega_{pe}/\Omega_c = 1$, $y_0 = 0.49$. Dotted lines represent the real part of the solution when it is complex. (b) Growth rates for the decays in fluid model, $\Gamma = \mathrm{Im}(x)$ vs. y. Solid line: $\alpha = 0.2$; dashed line: $\alpha = 0.3$; dotted dashed line: $\alpha = 0.4$.

have a linear growth, and performing a linear fit whose slope will correspond to the growth rate. This figure [Fig. 9(b)] shows a behavior that is similar to the one predicted by the fluid model [Fig. 9(a)]. The maximum of the growth rate lies in $y \approx 0.8 \sim 1$ and this growth rate increases as we increase α. We note that the instability in the simulation, Fig. 9(b), has a lower growth rate than predicted by the fluid model, which can be understood due to the presence of effects such as Landau damping, which is not present in a fluid model.

V. DEPENDENCE ON TEMPERATURE

In Ref. 35, the parametric decays were studied for various wave amplitude and plasma temperatures. In the fluid model, it was found that an increment in the plasma temperature μ results in a decrease of the maximum growth rate.[35] To study this behavior, in Fig. 10(a) we have plotted the dispersion relation of the decays in Ref. 35 for $\alpha = 0.2$ and $\mu = 50$, which is a larger temperature than used in the previous case. In this case, the same instabilities appear in a narrower range of wave number, and the growth rate, Fig. 10(b), is small in comparison to the previous case of Fig. 9(a).

In Fig. 11, we plot the dispersion relation and the growth rates of the density fluctuations in the simulation, for $\mu = 50$.

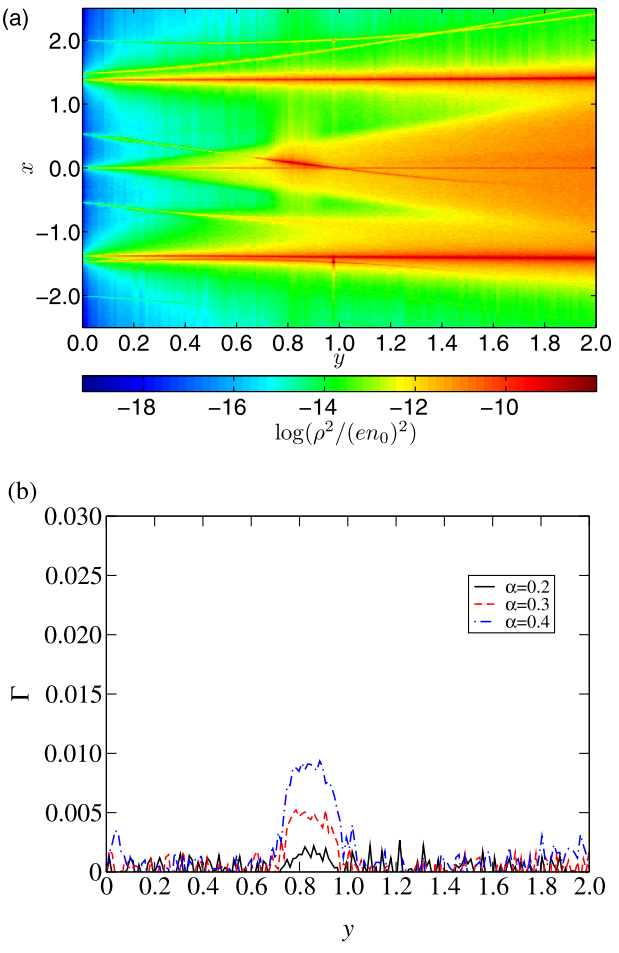

FIG. 11. Parametric decays in the simulation, for $\mu = 50$, $\omega_{pe}/\Omega_c = 1$, and taking average over 16 simulations. (a) Dispersion relation x vs. y for density fluctuations. (b) Growth rates for the density fluctuations modes in the simulation, $\Gamma = \mathrm{Im}(x)$ vs. y. Straight line: $\alpha = 0.2$. Dashed line: $\alpha = 0.3$. Dotted dashed line: $\alpha = 0.4$.

In Fig. 11(a), the dispersion relation shows most of the modes predicted by the fluid theory [Fig. 10]. The power is concentrated in the range of $y \approx 0.7 - 0.9$, which corresponds to the coupling (S_+, p_-), as in the previous case [Fig. 6(b)]. Fig. 11(b) shows that in this zone we have the largest instability, as in the previous case [Fig. 9]. Fig. 11(b) also shows that as we increase the pump wave amplitude, the instabilities become greater, in accordance with the fluid model, Fig. 10(b). Furthermore, the growth rate decreases with the temperature as expected from the fluid theory.

In Fig. 12, we observe the temporal evolution of the wave number modes. Fig. 12(a) shows the evolution of the electromagnetic modes. Here, the main active mode, for the whole period of the simulation, is the pump wave at $y = 0.49$, in comparison with the previous case of a lower temperature. The secondary mode is at $y \approx -0.3 \sim -0.5$ and corresponds to the p_- mode in the coupling (S_+, p_-). The mode S_+ can be seen in Fig. 12(b) at $y \approx 0.8$. The fact that growth rates are smaller in this case leads to the instability developing at later times as compared with Fig. 7(b). In effect, the S_+ mode in Fig. 12(b) begins to grow at $\omega_{pe}t \approx 800$, later than in Fig. 7(b), where the mode appears at about $\omega_{pe}t \approx 500$.

Now, we run the simulation for an even larger temperature $\mu = 10$. In the fluid model, Fig. 13, we can appreciate the same instabilities as in the previous cases, but with very small growth rates. From Fig. 13(a), we observe that the couplings (S_+, p_-) and (p_+, p_-) occur in a very narrow range of frequency and wave number, $(\omega, k) \approx (0.2, 0.6)$. Since these instabilities have very small growth rates, they will need

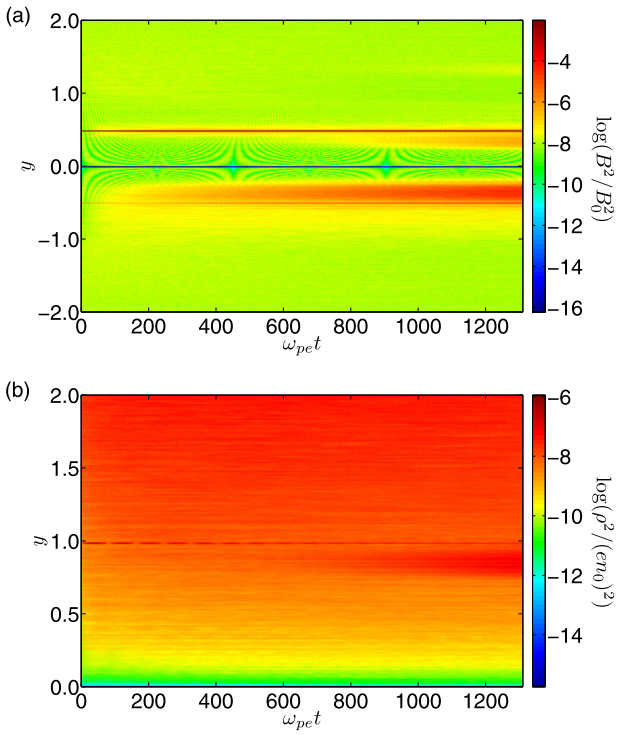

FIG. 12. Temporal evolution of the wave number modes, y vs. $\omega_{pe}t$. Both graphs for $\mu = 50$, $\alpha = 0.2$, $\omega_{pe}/\Omega_c = 1$, $y_0 = 0.49$, and taking average over 16 simulations. (a) Modes for the transverse magnetic fluctuations. (b) Modes for the density fluctuations.

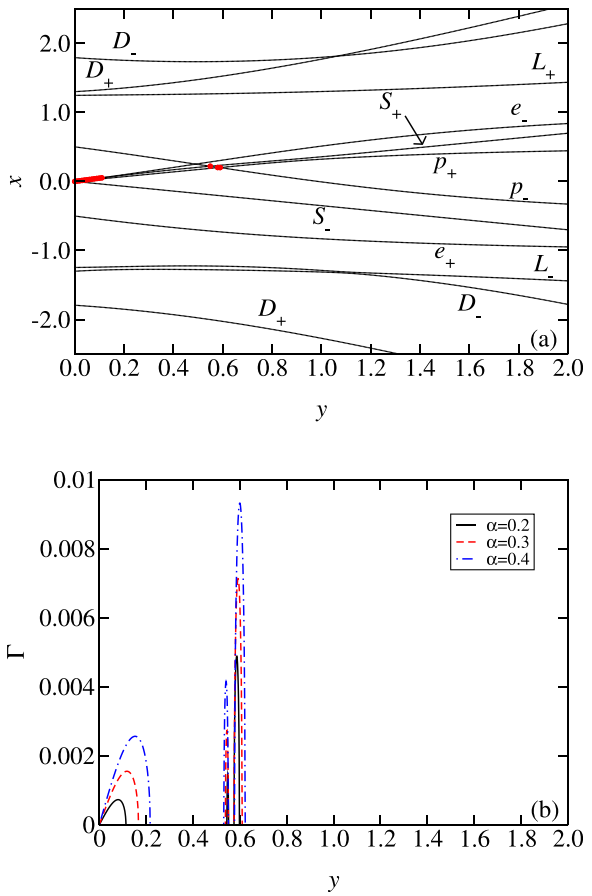

FIG. 13. Same as Fig. 10, but for a larger temperature. Parameters are $\mu = 10$, $\omega_{pe}/\Omega_c = 1$, $y_0 = 0.49$, (a) Dispersion relation x vs. y for fluid theory, Eq. (32) in Ref. 35, for $\alpha = 0.2$. Dotted lines represent the real part of the solution when it is complex. (b) Growth rates for the decays in fluid model, $\Gamma = \mathrm{Im}(x)$ vs. y. Solid line: $\alpha = 0.2$; dashed line: $\alpha = 0.3$; dotted dashed line: $\alpha = 0.4$.

more time to evolve, so we expect that they should appear at very large times in the simulation.

As in the first case considered here, we can plot the spatiotemporal evolution of the y component of the magnetic field in the simulation for this temperature $\mu = 10$, shown in Fig. 14. Here, the pump wave is the only wave propagating in the system during the entire simulation. If there are other decays, they are very damped and we cannot distinguish

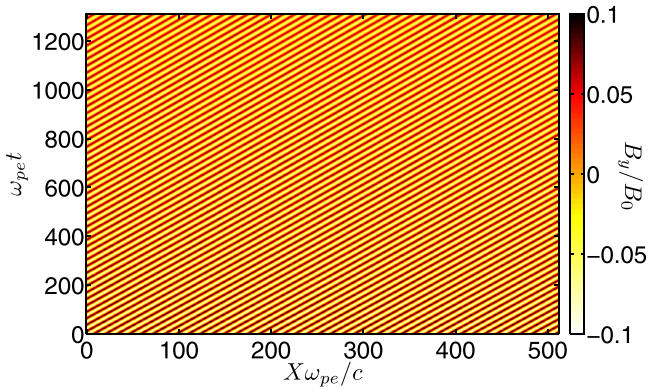

FIG. 14. Spatiotemporal evolution of the y component of the normalized magnetic field. Normalized time $\omega_{pe}t$ vs. normalized space $X\omega_{pe}/c$, for $\mu = 10$, $\alpha = 0.2$, $\omega_{pe}/\Omega_c = 1$, $y_0 = 0.49$ and x_0 lying in the Alfvén branch.

them in this figure. This result is consistent with the fluid theory as discussed above.

In Fig. 15, we have plotted the temporal evolution of the wave number for the plasma temperature $\mu = 10$. In the electromagnetic spectrum, Fig. 15(a), the power is concentrated in the pump wave number $y = 0.49$. The instabilities expected by the fluid theory have a very weak presence in this spectrum; it would be necessary more simulation time to let these instabilities evolve, because the expected growth rates of them are too small. However, we also notice that the modulational instability has a larger growth rate than the decay one, opposite to the fluid case [Fig. 13(b)]. This can be seen as an indication that, as the temperature is increased, the fluid model is increasingly inappropriate to describe the simulation results. However, location of the instabilities is still correctly given by the fluid results for this temperature.

Finally, we consider a very high plasma temperature $\mu = 1$ ($k_BT = mc^2$). From the fluid model, we expect no instabilities at all, as shown in Fig. 16. As discussed in Ref. 35, this is expected as a very large amplitude wave $\alpha > 1$ is needed to overcome the thermal motion of the particles.

In Fig. 17, the spatiotemporal evolution of the magnetic fluctuations is shown. The pump wave survives until about $\omega_{pe}t \approx 10$, and after that time it disappears due to the thermal motion of the particles. This behavior is not what we would expect from the fluid theory, and we see a clear kinetic effect as the thermal motion of the particles becomes relevant.

This means that the pump wave given by Eq. (4) cannot be regarded as a normal mode of the plasma for very large temperatures, and a model based on kinetic theory should be more appropriate.

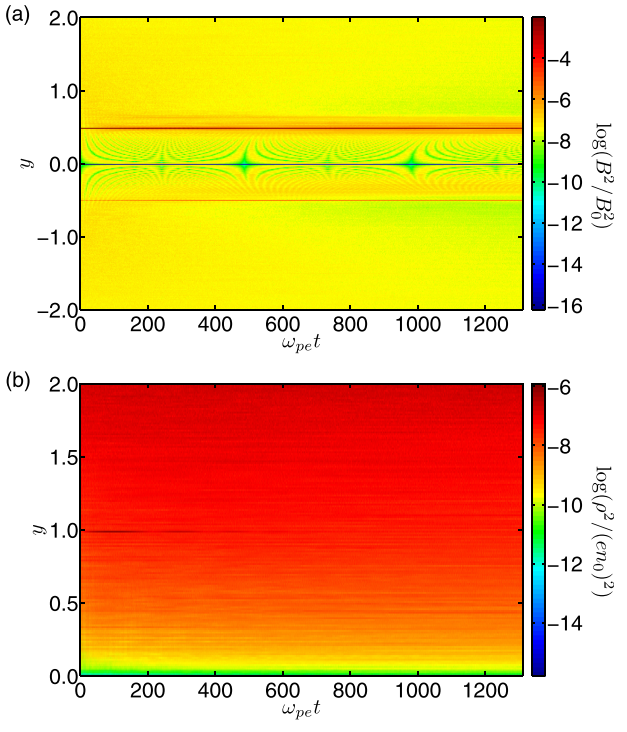

FIG. 15. Temporal evolution of the wave number modes, y vs. $\omega_{pe}t$. Both graphs for $\mu = 10$, $\alpha = 0.2$, $\omega_{pe}/\Omega_c = 1$, $y_0 = 0.49$, and taking average over 16 simulations. (a) Modes for the transverse magnetic fluctuations. (b) Modes for the density fluctuations.

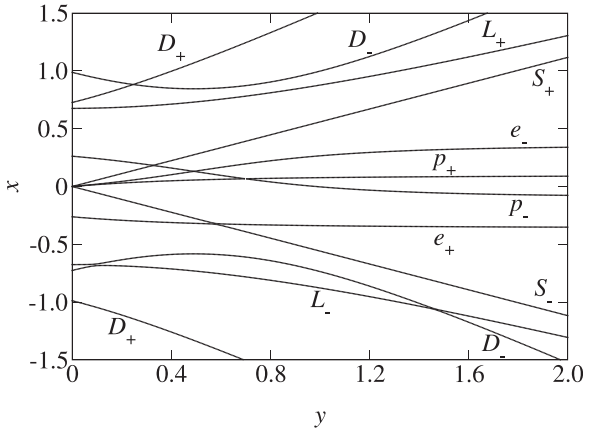

FIG. 16. Dispersion relation x vs. y for fluid theory, Eq. (32) in Ref. 35, for $\mu = 1$, $\alpha = 0.2$, $\omega_{pe}/\Omega_c = 1$, $y_0 = 0.49$.

Domínguez *et al.*[43] studied the propagation of a circularly polarized electromagnetic wave by means of a kinetic treatment in one dimension, based on the relativistic Vlasov equation. It was shown that the Alfvén branch is suppressed for large temperatures, and in particular for $\omega_{pe}/\Omega_c = 1$, the maximum value of the temperature for which the Alfvén branch still exists corresponds to $\mu = 2$. Thus, our results for $\mu = 1$ are consistent with the analysis in Ref. 43.

Hence, the situation in Fig. 17 is that an Alfvén wave is being forced to propagate in the system, but not being a normal mode for this, the wave is rapidly destabilized.

VI. CONCLUSIONS

We have studied the parametric decays of a left-handed circularly polarized Alfvén wave propagating along a constant background magnetic field in a relativistic electron-positron plasma with temperature, by means of a one dimensional relativistic PIC simulation. The results of the particle simulation have been compared with the predictions of the fluid model presented in Ref. 35.

For low temperatures, $\mu = 100$, the fluid model predicts various instabilities. The main instability in this case is a decay instability in which the pump wave decays into a forward propagating electroacoustic mode and a backward propagating electromagnetic wave, (S_+, p_-). There is also a modulation instability and a beat instability, but with a lower growth rate.

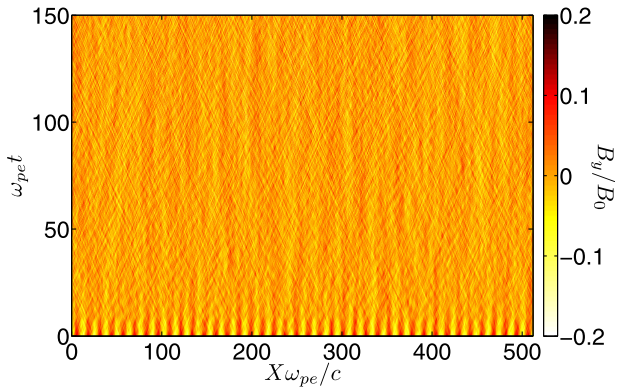

FIG. 17. Spatiotemporal evolution of the y component of the normalized magnetic field. Normalized time $\omega_{pe}t$ vs. normalized space $x\omega_{pe}/c$, for $\mu = 1$, $\alpha = 0.2$, $\omega_{pe}/\Omega_c = 1$, $y_0 = 0.49$.

We have run a simulation with the same parameters as in the fluid model in Sec. II. The results of the simulation show that the pump wave propagates in this plasma with the expected phase velocity, in the initial stage of the simulation. For larger times, we observe the appearance of instabilities. We can associate the major instabilities in the simulation with the ones predicted by the fluid theory, giving us a qualitatively close match between them in this range of temperatures. The growth rates for the instabilities in the simulation agree, in general, with the fluid theory, although in the simulation the growth rates are lower than in the fluid theory because in the latter there are no kinetic effects such as Landau damping.

The effect of the pump wave amplitude was also studied and the same behavior as in the fluid theory was found, so that an increase in the pump wave amplitude produces an increase in the growth rate of the instabilities.

As we consider larger temperatures, the same instabilities predicted by the fluid theory appear, but with smaller growth rates. In particular, for $\mu = 10$, the modulational instability has a larger growth rate than the decay one, opposite to the fluid case. This indicates that the fluid theory becomes inappropriate to describe the simulation results for larger temperatures, although location of the instabilities is still correctly given by the fluid model.

For very high temperatures, $\mu = 1$, the fluid model predicts that all the instabilities are suppressed. Instead, in the simulation, the pump wave vanishes in a very short time. This inconsistency between the simulation and the fluid model can be resolved by considering the relativistic kinetic treatment presented in Ref. 43, where Alfvén waves are suppressed for very high temperatures. In particular, Ref. 43 predicts that $\mu = 2$ is the minimum value of μ (maximum temperature) for which the Alfvén wave is a normal mode of the system for $\omega_{pe}/\Omega_c = 1$. For larger temperatures, there are no Alfvén waves. We have corroborated this prediction using a particle-in-cell simulation.

For a more appropriate comparison between theoretical models and particle simulations, we should consider the parametric decays based on a kinetic model treatment, such as Refs. 44–46.

ACKNOWLEDGMENTS

We thank the support of Conicyt through Fondecyt Grant Nos. 1110135 (J.A.V.), 1110729 (J.A.V.), 1080658, and 1121144 (V.M.). R.A.L. thanks the award of a Doctoral Fellowship from Conicyt, Contract No. 21100839, and for a Becas Chile fellowship, Contract No. 75120086, for a doctoral internship at NASA/GSFC. We also thank the support of Cedenna.

[1]M. F. Curtis, *The Theory of Neutron Stars Magnetospheres* (University of Chicago Press, Chicago, 1991).
[2]Y. N. Istomin and D. N. Sobyanin, Astron. Lett. **33**, 660 (2007).
[3]S. J. Hardy and M. H. Thoma, Phys. Rev. D **63**, 025014 (2000).
[4]C. S. Reynolds, A. C. Fabian, A. Celottid, and M. J. Rees, Mon. Not. R. Astron. Soc. **283**, 873 (1996).
[5]T. Piran, Phys. Rep. **314**, 575 (1999).

[6]T. Piran, Rev. Mod. Phys. **76**, 1143 (2005).
[7]*The Very Early Universe*, edited by G. W. Gibbons, S. Hawking, and S. T. C. Siklos, (Cambridge University Press, Cambridge, 1985).
[8]T. Tajima and T. Taniuti, Phys. Rev. A **42**, 3587 (1990).
[9]D. B. Blaschke, A. V. Prozorkevich, C. D. Roberts, S. M. Schmidt, and S. A. Smolyansky, Phys. Rev. Lett. **96**, 140402 (2006).
[10]G. P. Zank and R. G. Greaves, Phys. Rev. E **51**, 6079 (1995).
[11]P. Helander and D. J. Ward, Phys. Rev. Lett. **90**, 135004 (2003).
[12]Q. Luo, D. B. Melrose, and D. Fussell, Phys. Rev. E **66**, 026405 (2002).
[13]S. Iwamoto and F. Takahara, Astrophys. J. **565**, 163 (2002).
[14]J. F. C. Wardle, D. C. Homan, R. Ojha, and D. H. Roberts, Nature **395**, 457 (1998).
[15]J. T. Gosling, R. M. Skoug, D. J. McComas, and C. W. Smith, J. Geophys. Res. **110**, A01107, doi:10.1029/2004JA010809 (2005).
[16]T. D. Phan *et al*., Nature **439**, 175 (2006).
[17]A. C.-L. Chian and P. R. Muñoz, Astrophys. J. Lett. **733**, L34 (2011).
[18]C. H. Jaroschek, R. A. Treumann, H. Lesch, and M. Scholer, Phys. Plasmas **11**, 1151 (2004).
[19]M. Swisdak, Y.-H. Liu, and J. F. Drake, Astrophys. J. **680**, 999 (2008).
[20]S. Zenitani and M. Hoshino, Astrophys. J. **677**, 530 (2008).
[21]N. Bessho and A. Bhattacharjee, Astrophys. J. **750**, 129 (2012).
[22]B. Cerutti, G. R. Werner, D. A. Uzdensky, and M. C. Begelman, Astrophys. J. Lett. **754**, L33 (2012).
[23]J. Arons, Int. J. Mod. Phys. D **17**, 1419 (2008).
[24]M. Kino, N. Kawakatu, and F. Takahara, Astrophys. J. **751**, 101 (2012).
[25]G. Weidenspointner *et al*., Nature **451**, 159 (2008).
[26]T. S. Pedersen, J. R. Danielson, C. Hugenschmidt, G. Marx, X. Sarasola, F. Schauer, L. Schweikhard, C. M. Surko, and E. Winkler, New J. Phys. **14**, 035010 (2012).
[27]P. Goldreich and W. H. Julian, Astrophys. J. **157**, 869 (1969).
[28]A. N. Timokhin and J. Arons, Mon. Not. R. Astron. Soc. **429**, 20 (2013).
[29]A. K. Harding, Astrophys. J. **300**, 167 (1986).
[30]A. A. da Costa, D. A. Diver, and G. A. Stewart, Astron. Astrophys. **366**, 129 (2001).
[31]S. Matsukiyo and T. Hada, Astrophys. J. **692**, 1004 (2009).
[32]V. Muñoz and L. Gomberoff, Phys. Rev. E **57**, 994 (1998).
[33]S. Matsukiyo and T. Hada, Phys. Rev. E **67**, 046406 (2003).
[34]R. Svensson, Astrophys. J. **258**, 335 (1982).
[35]R. A. López, F. A. Asenjo, V. Muñoz, and J. A. Valdivia, Phys. Plasmas **19**, 082104 (2012).
[36]F. A. Asenjo, V. Muñoz, J. A. Valdivia, and T. Hada, Phys. Plasmas **16**, 122108 (2009).
[37]F. Jüttner, Ann. Phys. **339**, 856 (1911).
[38]P. L. Pritchett, Space Sci. Rev. **42**, 17 (1985).
[39]H. Matsumoto and Y. Omura, *Computer Space Plasma Physics: Simulation Techniques and Software* (Terra Scientific, Tokyo, 1993).
[40]*Advanced Methods for Space Simulations*, edited by H. Usui and Y. Omura (Terra Scientific, Tokyo, 2007).
[41]T. Terasawa, M. Hoshino, J.-I. Sakai, and T. Hada, J. Geophys. Res. **91**, 4171, doi:10.1029/JA091iA04p04171 (1986).
[42]M. Longtin and B. U. Ö. Sonnerup, J. Geophys. Res. **91**, 6816, doi:10.1029/JA091iA06p06816 (1986).
[43]M. Domínguez, V. Muñoz, and J. A. Valdivia, Phys. Rev. E **85**, 056416 (2012).
[44]V. Muñoz and L. Gomberoff, Phys. Plasmas **9**, 2534 (2002).
[45]V. Muñoz and L. Gomberoff, Phys. Plasmas **9**, 4415 (2002).
[46]V. Muñoz, T. Hada, and S. Matsukiyo, Earth, Planets Space **58**, 1213 (2006).